RSC Advances

PAPER

View Article Online
View Journal | View Issue

Cite this: *RSC Adv.*, 2022, **12**, 16257

Hierarchical hollow-tubular porous carbon microtubes prepared *via* a mild method for supercapacitor electrode materials with high volumetric capacitance

Xuan Xiao,[a] Lei Song,[a] Qianli Wang,[a] Zhicheng Wang,[a] Hongyan Wang,[a] Juncai Chu,[a] Jianmin Liu,[a] Xinru Liu,[a] Zhentao Bian *[ab] and Xuanxuan Zhao[c]

In this paper, hollow-tubular porous carbons were synthesized from abundant biomass Cycas fluff (CF) through simple carbonization followed by an $NaHCO_3$ mild activation process. After activation, the tubular structure of the CF was retained, and a hierarchical structure of micropores, mesopores and macropores was formed. When the optimal mass ratio of $NaHCO_3$/CF is 2, the obtained porous carbon CF-HPC-2 sample has a large specific surface area (SSA) of 516.70 $m^2\ g^{-1}$ in Brunauer–Emmett–Teller (BET) tests and a total pore volume of 0.33 $cm^3\ g^{-1}$. The C, O, N and S contents of CF-HPC-2 were tested as 91.77 at%, 4.09 at%, 3.54 at%, and 0.6 at%, respectively, by elemental analysis. Remarkably, CF-HPC-2 exhibits a high volume capacitance (349.1 F cm^{-3} at 1 A g^{-1}) as well as a higher rate capability than other biomass carbon materials (289.1 F cm^{-3} at 10 A g^{-1}). Additionally, the energy density of the CF-HPC-2 based symmetric supercapacitor in 2 M Na_2SO_4 electrolyte at 20 kW kg^{-1} is 27.72 W h kg^{-1}. The particular hollow tubular morphology and activated porous structure determine the excellent electrochemical performance of the material. Hence, this synthetic method provides a new way of storing energy for porous carbon as high volumetric capacitance supercapacitor materials.

Received 2nd April 2022
Accepted 20th May 2022

DOI: 10.1039/d2ra02141b

rsc.li/rsc-advances

1 Introduction

For the past few years, the risks associated with global warming and the continued increase in CO_2 emissions caused by the massive emission of greenhouse gases from the burning of fossil fuels have attracted worldwide attention.[1–3] A large number of new energy sources are being developed, resulting in a growing demand for eco-friendly, efficient, and low-cost energy storage technologies.[4–8] However, compared with traditional capacitors, supercapacitors are a type of electrochemical energy storage equipment associated with low cost, high power density, stable cycling life, and good operational stability.[9,10] However, supercapacitors have the problems of high cost and poor electrical conductivity in commercial applications. In order to solve this problem, the development of high-efficiency carbon electrode materials that exhibit high energy has been researched.[11,12]

Currently, the commonly used electrode materials for supercapacitors mainly include porous carbon, carbon nanotubes, graphene, and other carbon-based materials.[13,14] Among them, porous carbon has the advantages of a hierarchical porous structure, a high surface area and good cycling stability.[15,16] As far as we know, constructing a hierarchical porous structure significantly improves the electrochemical performance of porous carbon.[17,18] The well-defined hierarchical porous structure not only provides efficient and stable channels for rapid diffusion/transfer, but also offers a higher specific surface area (SSA).[19,20] Besides this, introducing heteroatoms (such as N, S) to the framework and surface of porous carbon can produce additional pseudo-capacitance,[21–23] as well as facilitate conductivity and surface wettability.[24–26] Research has shown that porous carbon that has been co-doped exhibits better electrochemical properties due to the synergistic effect of the self-doped heteroatoms.[27,28] Various methods have been used for preparing porous carbon materials, including the catalytic activation of biowaste, chemical vapor deposition, *etc.*[29,30] Nevertheless, the cumbersome multi-step procedures, complex process conditions and expensive precursor consumption hinder the large-scale production of porous carbon.[31]

The raw materials for the production of porous carbon are coal[32] and asphalt,[33] but considering the excessive consumption

[a]*Anhui Key Laboratory of Spin Electron and Nanomaterials (Cultivating Base), Bio-based Functional Materials and Composite Technology Research Center, School of Chemistry and Chemical Engineering, Suzhou University, Suzhou 234000, PR China. E-mail: zhentaobian@ahszu.edu.cn*

[b]*Chemical Technology, Institute of Chemical Technology, China University of Mining &Technology, XuZhou, Jiangsu 221116, PR China*

[c]*Suzhou Yifan Pharmaceutical Co., Ltd., Suzhou 234000, PR China*

of fossil fuels and some environmental problems, biomass as a raw material has entered the field of vision of researchers. Because of its advantages of low cost, being a complete source, environmental friendliness and many self-doped heteroatoms, the preparation of porous carbon using biomass as a precursor is becoming increasingly more popular.[34] Jiang *et al.*[16] used natural cotton fiber as a raw material and coated it with NaH_2PO_4 to successfully prepare a hollow tubular porous material *via* simple carbonization and KOH–KNO_3 activation. Zhou *et al.* prepared a hollow tubular structure with corn silk as a raw material *via* a one-step carbonization method. After KOH activation, a hierarchical porous structure with a high surface area and heteroatom doped content was obtained.

Chemical reagents promote dehydration and the structural reorganization of the pores of carbonaceous materials. Various chemical reagents can be used as activators, namely salts of alkali metals ($AlCl_3$, $ZnCl_2$),[35] acids (H_3PO_4,[36] H_2SO_4), or bases (KOH, NaOH, K_2CO_3, Na_2CO_3).[37–39] Zinc chloride is the main chemical activator used on a large scale. It has now been abandoned due to environmental problems linked to the toxicity of residual zinc-derived compounds. Magnesium chloride produces toxic gases that are harmful to the human body and the environment during experiments. Phosphoric acid (H_3PO_4) easily generates various forms of phosphate and phosphite at high temperature, so that the ash content of activated carbon increases. Compared with H_3PO_4, KOH is highly corrosive to instruments. Therefore, KOH is rarely used to synthesize porous carbon in industrial production. $NaHCO_3$ is weakly alkaline and is milder, more environmentally friendly and safer than other chemical activators, therefore making $NaHCO_3$ a beneficial activator for the preparation of gradient porous carbon.[40] As an activator, $NaHCO_3$ produce more micropores and mesopores, which is beneficial to increasing the SSA. Therefore, $NaHCO_3$ is one of the most suitable activators.

Hence, we use Cycas fluff (CF) as a carbon material and $NaHCO_3$ as an activator to synthesize hollow-tubular porous carbon *via* a simple approach. The results show that the prepared porous carbon not only retains the hollow tubular structure of the original fibers, but also forms a hierarchical porous structure. CF-HPC-2 sample has a relatively high SSA of 516.70 $m^2\ g^{-1}$ and a total volume of 0.33 $cm^3\ g^{-1}$. Remarkably, the obtained porous carbon exhibits a high volume capacitance of 349.1 F cm^{-3} at 1 A g^{-1} and 289.1 F cm^{-3} at 10 A g^{-1}, and high-performance carbon with rich energy groups was produced. The regulation and development of high-performance, low-cost and green porous carbon electrode materials from biomass materials not only alleviates the increasingly severe energy crisis, but also solves the problems of environmental pollution and energy storage.

2 Experimental

2.1 Materials

Cycas fluff was collected Suzhou University, Anhui Province, China. Sodium bicarbonate ($NaHCO_3$), hydrogen chloride (HCl), and ethanol were purchased from Aladdin Chemistry (China) Co., Ltd. None of the chemicals underwent any purification. Deionized water was used during the whole process.

2.2 Preparation of CF-0 and CF-HPC-*y*

The preparation steps of CF-0 and CF-HPC-*y* are illustrated in Fig. 1. CF-HPC-*y* was prepared using CF as a precursor and $NaHCO_3$ as an activator. The CF was cleaned with distilled water and dried and then completely immersed in an aqueous $NaHCO_3$ solution for 24 h in a weight ratio of $NaHCO_3$: CF = 0 : 1, 1 : 1, 2 : 1, and 3 : 1, before being further dried at 100 °C for 24 h. Then, the CF was activated at 700 °C under an Ar atmosphere for 2 h at a heating rate of 5 °C min^{-1}. The samples were finally washed using 1 M HCl and then washed (with deionized water) to eliminate the $NaHCO_3$, until the pH value of the solution reached about 7. The resulting samples were dried at 100 °C for 24 h. According to the weight ratio of $NaHCO_3$: CF, the products obtained were named CF-0, CF-HPC-1, CF-HPC-2, and CF-HPC-3.

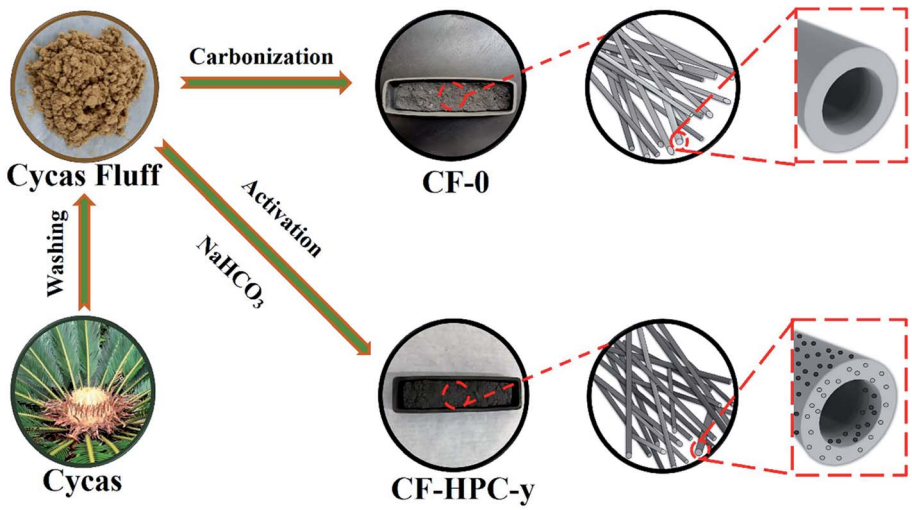

Fig. 1 Schematic illustrations of the preparation of CF-0 and CF-HPC-*y* from Cycas fluff.

2.3 Characterization

Scanning electron microscopy (SEM, Hitachi S-2600N) and transmission electron microscopy (TEM, JEOL JE-2100F) were used to study the structural properties and morphology of the composite. The crystal structure was tested using an X-ray diffraction analyzer (XRD, Smartlab 9 kW, Japan). The XRD results were further verified by Raman spectroscopy (Thermo Fisher). The nitrogen adsorption/desorption isotherms were tested on a Micromeritics ASAP 2020 analyzer. The BET surface area was assessed and the T-plot method was used to calculate pore size distribution. Surface elements were analyzed by XPS measurements (XPS, 250Xi, Thermo Fisher Escalab, USA).

2.4 Electrochemical measurements

Firstly, the as-prepared carbon samples, acetylene black and PTFE with a mass ratio of 48 : 9:3 were mixed with ethanol. The above mixture in ethanol solvent was coated onto 1 × 1 cm^2 nickel foam and dried at 85 °C for 24 h (the loading density of the electrode was controlled to be *ca.* 2.5 mg cm^{-2}). The electrochemical performance of CF was then measured in 6 M KOH electrolyte using a three-electrode cell system on an electrochemical workstation (CHI760D). The electrochemical performances of the samples were measured using a carbon rod and Hg/HgO as counter and reference electrodes, respectively. Cyclic voltammetry (CV), galvanostatic charge–discharge (GCD) and electrochemical impedance spectroscopy (EIS) were measured on an electrochemical workstation at room temperature. CV performance was tested in the potential range of −1 to 0 V, EIS measurements of the supercapacitor were conducted within a frequency domain of 100 kHz to 0.01 Hz. The gravimetric capacitance (C, F g^{-1}) and volumetric capacitance (C_v, F cm^{-1}) were measured according to:

$$C = (I \times \Delta t)/(m \times \Delta V) \quad (1)$$

$$C_v = C \times \rho \quad (2)$$

$$\rho = 1/[V_t + (1/\rho_t)] \quad (3)$$

In these formulas, I (A), Δt (s), m (g), and ΔV (V) are the discharge current, discharge time, mass of the active materials, and working potential range, respectively. ρ_t is the true density of carbon (2 g cm^{-3}),[41] ρ (g cm^{-3}) is the density of CF and V_t is the total pore volume (cm^3 g^{-1}).

The electrochemical performance of the CF-HPC-2//CF-HPC-2 device was realized in a two-electrode electrochemical test system. The working electrodes were prepared using the same method as that for the working electrode in three-electrode system. Symmetric two-electrode cells were assembled using two electrodes with exactly the same mass and were conducted in the voltage range of 0–2.0 V. The specific capacitances (C_s, F g^{-1}), energy density (E, Wh kg^{-1}) and power density (P, W kg^{-1}) were determined separately according to:

$$C_s = (4I \times \Delta t)/(m \times \Delta V) \quad (4)$$

$$E = (C_s \times \Delta V^2)/(2 \times 3.6) \quad (5)$$

$$P = 3600 \times E/\Delta t \quad (6)$$

where I (A) is the discharge current, m (g) refers to the total mass of active materials on both electrodes, ΔV is the potential difference (V) in the discharge process, and Δt is the discharge time (s).

3 Results and discussion

The surface morphology of the dried CF was investigated by SEM, as shown in Fig. 2a and b. A long tubular structure with slight folds was observed. The effect of different $NaHCO_3$ content on the morphology and structure of the CF was studied. As can be seen, CF-0 exhibits a slender, smooth and hollow tubular structure without obvious holes or damage (Fig. 2c). The CF-HPC-1 sample is tubular with an abundant hierarchical porous structure and presents coarse surface particles, as shown in Fig. 2d. Owing to $NaHCO_3$ activation and carbonization, the tubular structure of CF was destroyed and formed an apparent porous structure. After activation by $NaHCO_3$, more intense damage occurs on the tubular structure, leaving a rough surface on CF-HPC-2 (Fig. 2e). Retaining the hollow elongated framework is essential for ion diffusion/transport, meanwhile the abundant pores can facilitate electrolyte penetration and offer more electrochemically active sites. Interestingly, CF-HPC-3 presents a large collection of irregular broken block particles with a coarse surface (Fig. 2f), probably due to the destruction of etched pores induced by the high $NaHCO_3$ dosage.

The microstructure of CF-HPC-2 was further studied by transmission electron microscopy, as shown in Fig. 3. Fig. 3a and b show the relatively sharp edges of the thin carbon sheet interconnected with porous structures that resemble wormholes. The surface of CF-HPC-2 shows a highly stratified micropore arrangement, with micropores (<2.0 nm), mesopores (2.0–50.0 nm) and macropores (>50.0 nm) (Fig. 3c and d). The porosity of the carbon material is critical to the rapid migration and infiltration of electrolyte ions. Obviously, a material with a hierarchical pore structure like CF-HPC-2 can be expected to have good electrochemical performance. Additionally, elemental mapping was carried out to examine elements present in CF-HPC-2, and also to confirm the uniformity of the C, N, O and S atom distribution on the surface of CF-HPC-2 (Fig. 3f–i). From elemental mapping, it was shown that the C, N, O and S atoms are homogeneously distributed on the surface of carbon matrix.

The chemical components of the CF samples were measured by X-ray photoelectron spectroscopy (XPS) (Fig. 4 and Table 1). As shown in Fig. 4a, the full scan spectra show four peaks at around 284, 532, 400 and 168 eV, indicating the existence of C, O, N and S respectively, in CF-0 and CF-HPC-*y*. Three individual peaks in the high-resolution C 1s spectrum in Fig. 4b at 284.7, 284.8, 286.3 eV can be attributed to C=C, C–C and C–O,[42,43] respectively. The deconvoluted O 1s spectrum (Fig. 4c) of CF-HPC-2 indicate the presence of three types of bonding at 531.9, 532.8 and 532.8 eV, corresponding to C=O, C–OH and C–O–C, respectively. These carbonyl (C=O) and hydroxyl (C–OH) functional groups participate in electrochemical redox

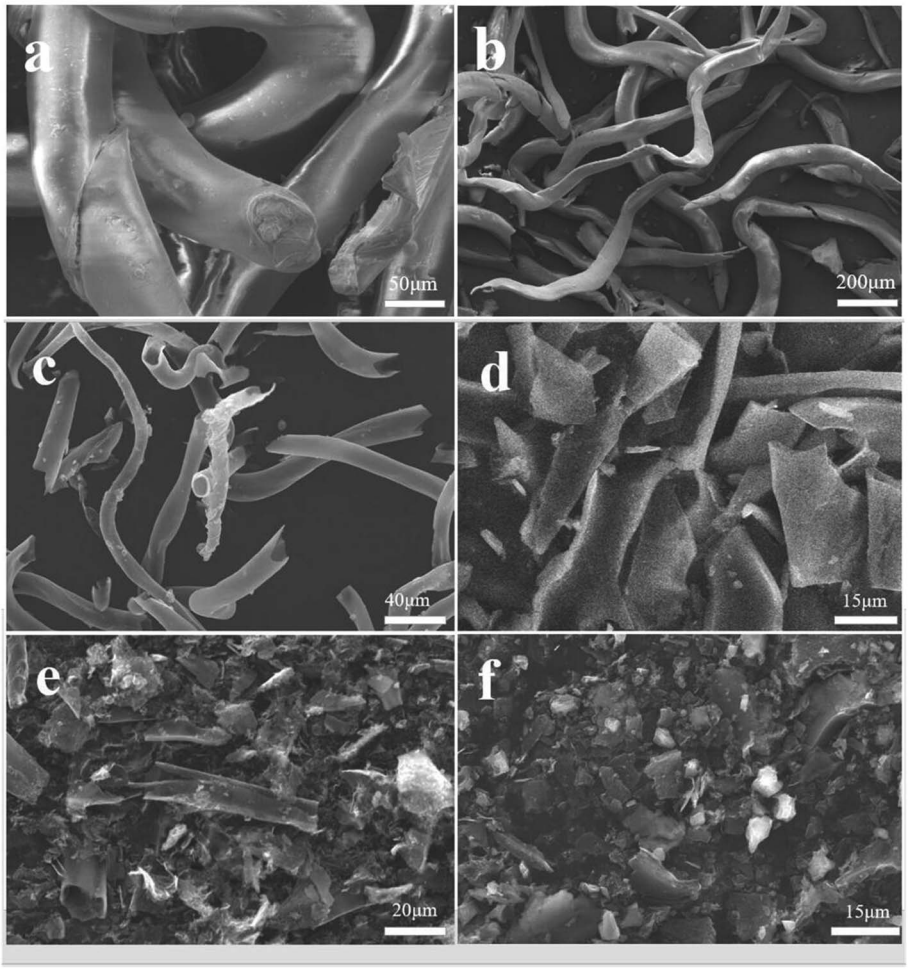

Fig. 2 SEM images of dried (a and b) CF, (c) CF-0, (d) CF-HPC-1, (e) CF-HPC-2, and (f) CF-HPC-3.

reactions which enhance the pseudo-capacitance: $\rangle$C–OH $\rightleftharpoons$ $\rangle$C=O + H^+ + e^-, $\rangle$C=O + e^- $\rightleftharpoons$ $\rangle$C–O– [44,45] The N 1s XPS region spectrum is shown in Fig. 4d, with three component peaks at 397.5, 400.3, and 402.5 eV, attributed to N-5, N-Q and N-X,[46] respectively. The presence of functional groups like N-5, N-Q and N-X enhances the energy storage performance of the material by providing pseudo-capacitive reactive sites. In addition, three distinguishable peaks in the spectrum of S 2p (Fig. 4e) at 163.6 eV, 164.7 eV and 168.5 eV correspond to –C–S–C–, –C=S– and –C–SO_x–C–, respectively.[44] Altogether, the O, N and S self-doped heteroatoms can availably enhance the electrochemical capacitance by improving the reversibility of the redox reactions and improving surface wettability and compatibility, thus exhibiting promising high-capacity storage performance.

XRD and Raman spectroscopy were employed to investigate the structures of CF-0 and CF-HPC-*y*. The XRD patterns show two diffraction peaks at around 24° and 44°, which are attributed to the reflections from the (002) and (100) planes of graphitic carbon (Fig. 5a).[47] Meanwhile, with an increase in $NaHCO_3$ content, the intensity of the (002) peak weakens, suggesting a low degree of graphitic structure.[48]

Fig. 5b displays the Raman spectra of the carbon samples. Two obvious characteristic Raman peaks can be observed distinctly at around 1333 cm^{-1} and 1594 cm^{-1}, respectively belonging to the D- and G-bands of disordered carbon and graphitic phase carbon.[49] Generally, the peak intensity ratio I_D/I_G is used as an indicator of structural defects in carbon-based samples. The I_D/I_G values of CF-0, CF-HPC-1, CF-HPC-2 and CF-HPC-3 were calculated to be 0.82, 0.91, 0.91 and 0.97, respectively. Clearly, the I_D/I_G value of CF-HPC-*y* samples is slightly higher than that of CF-0, suggesting that more structural defects were introduced into the CF-HPC-*y* samples as a result of $NaHCO_3$ activation, in agreement with the SEM results.

The pore structure properties of CF-0 and CF-HPC-*y* were studied by conducting N_2 adsorption/desorption measurements on the CF-HPC-*y* samples, which show representative type-I isotherms combined with typical IV type isotherms with a hysteresis of H4 type (Fig. 6).[50–52] It is clear that the sharp steep curves in the low P/P_0 (below 0.1) region indicate the characteristics of the monolayer adsorption of micropores. The hysteresis loop at P/P_0 in the range of 0.45–0.9 indicates the existence of a large amount of mesopores in the structure. Obviously, CF-HPC-*y* possesses a hierarchical porous structure

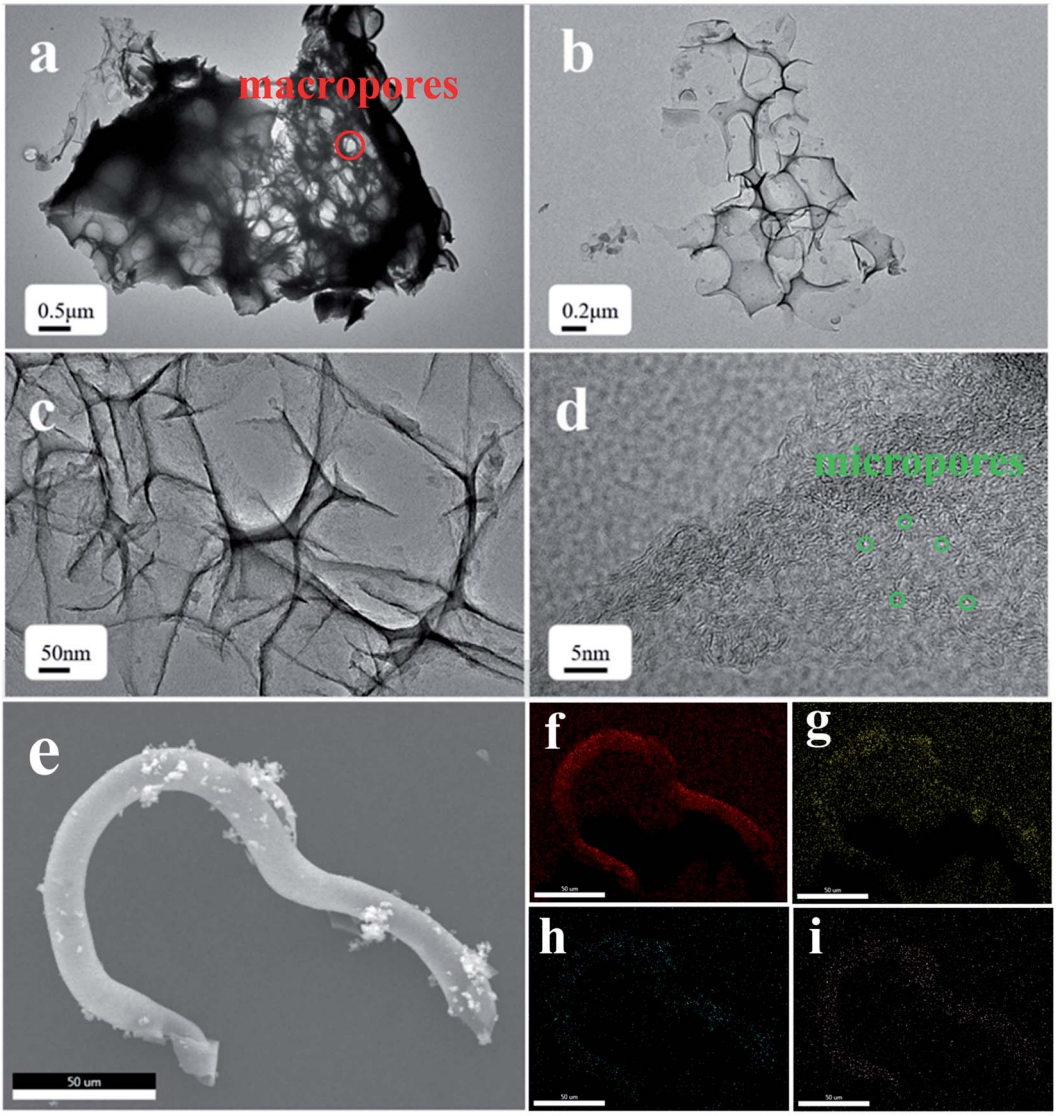

Fig. 3 TEM images at different magnifications of the (a–d) CF-HPC-2 samples, (e) SEM image and elemental mapping images of (f) C, (g) O, (h) N and (i) S for CF-HPC-2.

with a mixture of micropores and mes/macropores. After activation, the pore size distribution of the CF-HPC-*y* broadens, and the SSA and pore volume of the CF-HPC-1 slightly increase, which can be attributed to the increase in $NaHCO_3$ content. According to Table 2, when the proportion of $NaHCO_3$ increases to 1 : 3, the SSA and pore volume of CF-HPC-3 reduce drastically due to the destruction of the structure caused by excessive $NaHCO_3$. The BET surface areas of the CF-0, CF-HPC-1, CF-HPC-2, and CF-HPC-3 samples are 71.69, 377.94, 516.70 and 397.92 $m^2\ g^{-1}$, respectively.

To compare the electrochemical performance of the CF-0 and CF-HPC-*y* samples, the electrochemical properties of CF-0 and CF-HPC-*y* in three-electrode systems in 6 M KOH aqueous solution were studied using CV, GCD and EIS methods. Fig. 7a and b depicts the CVs and GCD tests of CF-0 and CF-HPC-*y*. The CV curves of CF-0 and CF-HPC-*y* show the main capacitance characteristics of a double layer capacitor (EDLC), and the pseudo-capacitance characteristics according to the approximate rectangular shape data with a few peaks. Nevertheless, CF-HPC-2 has a higher area than the other samples, indicating that its maximum capacitance supports it having the highest SSA and pore volume among the samples. The GCD testing of CF-0 and CF-HPC-*y* was also carried out, and the discharge time of CF-HPC-2 was significantly greater than those of the other samples, which is consistent with the CV results. To further explore the rate capability, the capacitance and discharge current density data of CF-0 and CF-HPC-*y* are shown in Fig. 7c. Obviously, CF-HPC-*y* has a higher capacitance (from 0.5 A g^{-1} to 10 A g^{-1}) compared to CF-0, indicating that CF-HPC-2 has superior rate capability (Table 3). CV of CF-HPC-2 under different scan rates and GCD under different current densities were studied. Fig. 7d displays CV curves of CF-HPC-2 in the scan rate range of between 5 and 100 mV s^{-1}. The quasirectangular CV curves were well maintained, even at 100 mV s^{-1}, implying

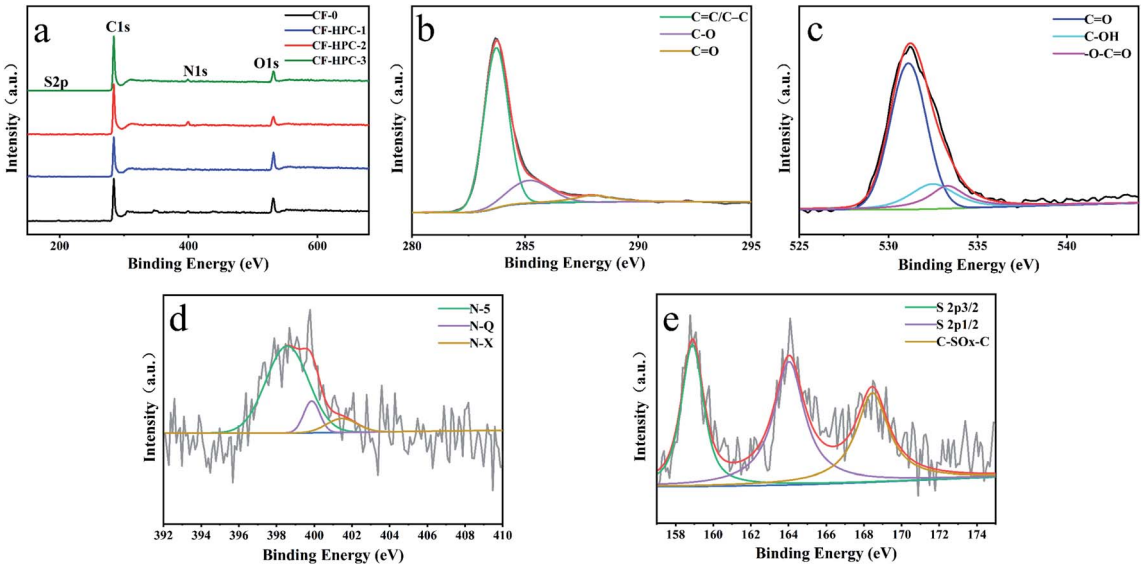

Fig. 4 Full scan spectra of (a) CF-0 and CF-HPC-*y* and (b–e) high-resolution C 1s, O 1s, N 1s and S 2p XPS spectra of CF-HPC-2.

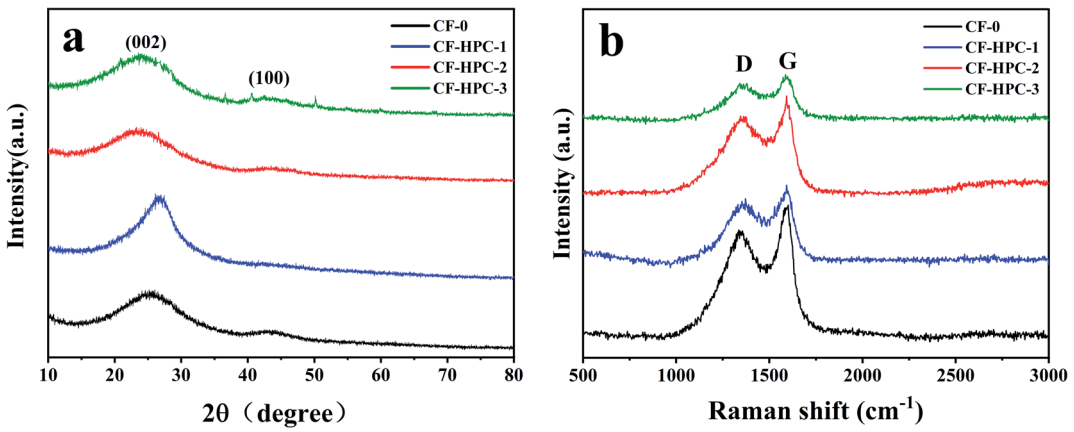

Fig. 5 (a) XRD patterns and (b) Raman spectra of CF-0 and CF-HPC-*y*.

Table 1 Elemental contents of CF and CF-HPC-*y*

	XPS (at%)			
Sample	C	N	O	S
CF	89.09	8.51	1.47	0.93
CF-HPC-1	85.85	11.64	1.58	0.93
CF-HPC-2	91.77	4.09	3.54	0.60
CF-HPC-3	92.92	4.83	1.78	0.47

the capacitive superiority of CF-HPC-2. Even at 10 A g^{-1}, the GCD data (Fig. 7e) exhibit an approximate triangular shape, further demonstrating the highest rate capability and excellent capacitive behavior of CF-HPC-2.

Afterward, the charge transport and accessibility of ions within the hierarchical architectures were verified by EIS testing. As shown in Fig. 7f, compared with CF-0, the Nyquist plot of CF-HPC-2 exhibits a nearly vertical plot in the low-frequency region (<0.1 Hz), revealing its ideal capacitive behavior, and it having the smallest semicircle at high frequency manifests that it exhibits the lowest charge transfer resistance, further demonstrating that CF-HPC-2 has the fastest ion spread and charge transfer ability in the electrolyte. The excellent electrochemical performance of CF-HPC-2 can be attributed to the following reasons. First of all, the large number of micropores generated during the activation process is the key to the EDLC properties. In addition, micropores shorten the length of the ion diffusion path. Secondly, mesopores provide ion transport channels, while macropores act as ion buffers. Lastly, the high specific surface area provides a large number of active sites for electrochemical reactions where charges are stored.

The electrochemical performance of CF-0 and CF-HPC-*y* in 1 M Na_2SO_4 aqueous solution in three-electrode system was also studied by the same method. It was observed that the CV curves of the CF-0 and CF-HPC-*y* electrodes exhibit a quasi-rectangular

Table 2 Pore parameters of CF-0 and the CF-HPC-*y* samples

Sample	S_{BET} ($m^2\ g^{-1}$)	S_{micro} ($m^2\ g^{-1}$)	S_{micro}/S_{BET} (%)	V_t ($cm^3\ g^{-1}$)	V_{micro} ($cm^3\ g^{-1}$)	V_{micro}/V_t (%)	ρ ($g\ cm^{-3}$)
CF-0	71.69	—	—	0.03	—	—	—
CF-HPC-1	377.94	273.54	72.38	0.21	0.15	71.43	1.41
CF-HPC-2	516.70	268.31	51.93	0.33	0.14	42.42	1.20
CF-HPC-3	397.92	310.56	78.05	0.23	0.17	73.91	1.37

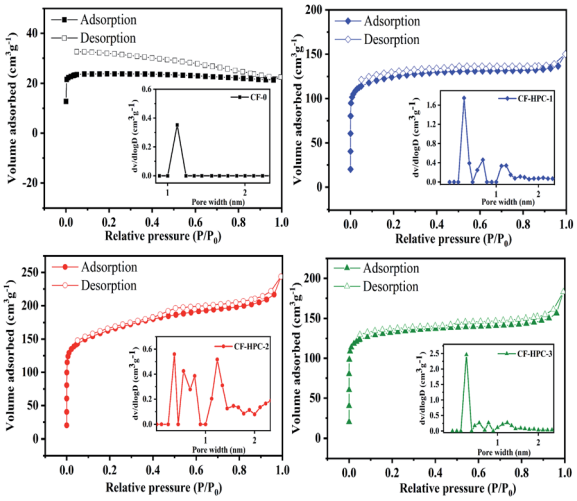

Fig. 6 N_2 adsorption–desorption isotherms obtained using the BET method and the pore-size distribution curves (inset) of CF-0 and the CF-HPC-*y* samples.

shape (Fig. 8a). The corresponding GCD curves of CF-0 and CF-HPC-*y* illustrated in Fig. 8b exhibit almost symmetrical triangular shapes, indicating reversible and typical electric double layer capacitor behavior. According to the Nyquist diagram of the sample (Fig. 8c), the curve of the CF-HPC-2 sample is more vertical at low frequency, showing a lower charge transfer resistance. The intercept on the Z' axis in the high frequency region is the lowest, indicating that the conductivity of CF-HPC-2 is better than those of the other samples. The CV plots of the CF-HPC-2 electrode at different scan rates were also measured, as shown in Fig. 8d, from which it can be seen that all the curves present a similar rectangular shape. All of the curves of CF-HPC-2 at various current densities (0.5 to 5 A g^{-1}) are almost symmetrical and linear, as shown in Fig. 8e. In addition, after 10 000 cycles, 96.36% and 96.71% of the initial specific capacitance were retained, respectively in Na_2SO_4 and KOH electrolyte, indicating that the electrode material has good cycling stability (Fig. 8f).

CF-HPC-2 was assembled into symmetric supercapacitors in 2 M Na_2SO_4 and 6 M KOH electrolyte solutions for further

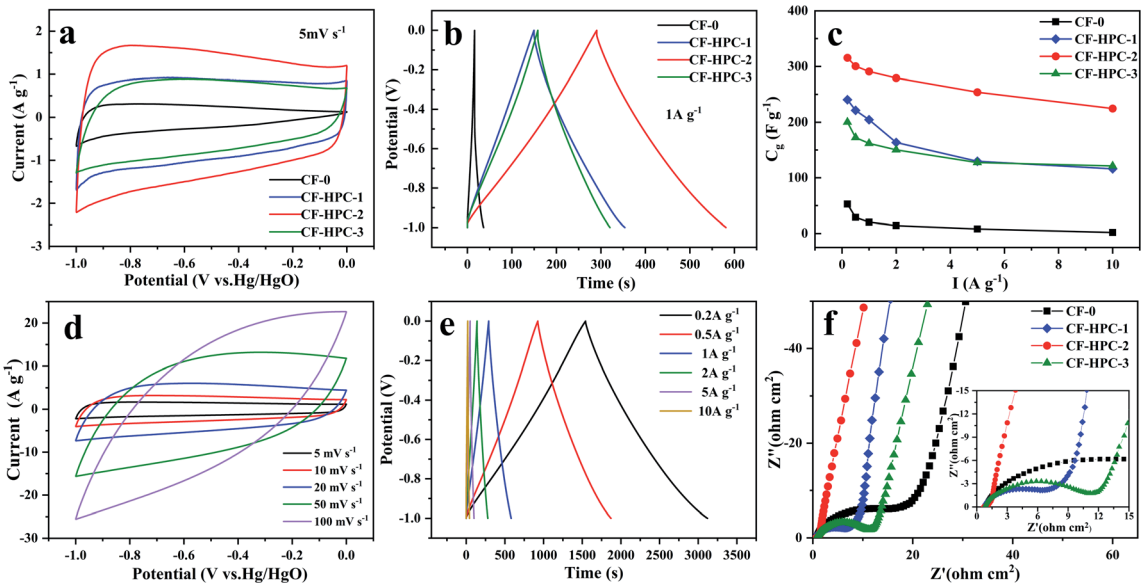

Fig. 7 Electrochemical properties of CF-0 and CF-HPC-*y* tested in a three-electrode system in 6 M KOH: (a) CV curves at a scan rate of 5 mV s^{-1}, (b) GCD curves at 1 A g^{-1}, (c) the specific capacitances of CF-0 and CF-HPC-*y* at current densities of 0.2–10 A g^{-1}, (d) CV curves of CF-HPC-2 at different scan rates, (e) GCD curves of CF-HPC-2 at 0.2–10 A g^{-1}, and (f) Nyquist plots.

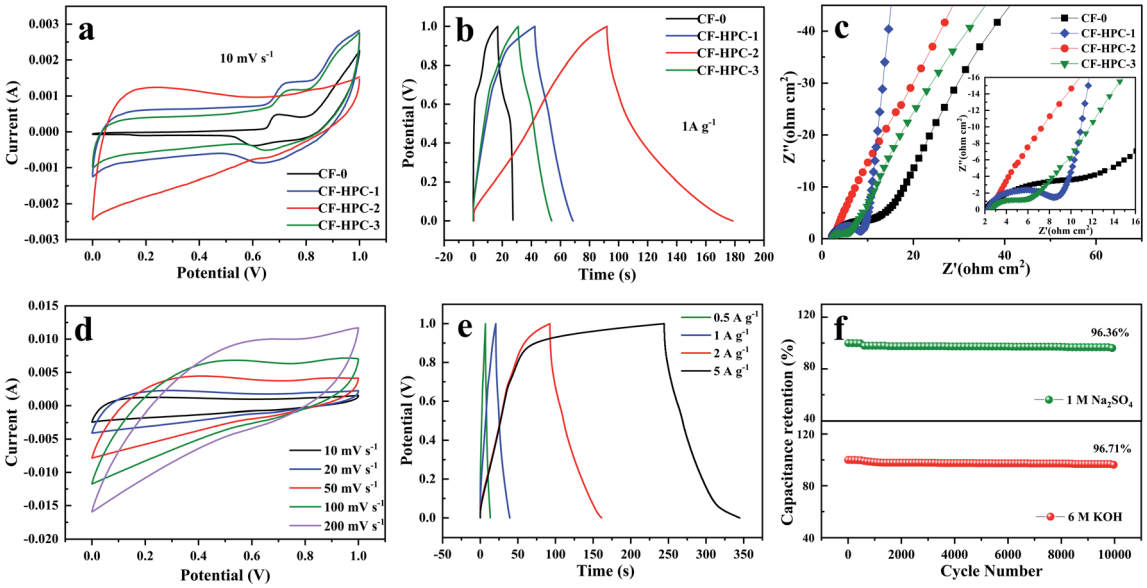

Fig. 8 Electrochemical performance of CF-0 and CF-HPC-*y* tested in a three-electrode system in 1 M Na_2SO_4: (a) CV curves at a scan rate of 10 mV s^{-1}, (b) GCD curves at 1 A g^{-1}, (c) Nyquist plots, (d) CV curves of CF-HPC-2 at different scan rates, (e) GCD curves of CF-HPC-2 at 0.5–5 A g^{-1}, and (f) Capacitance retention of CF-HPC-2 at 1 A g^{-1} in Na_2SO_4 and KOH electrolyte, respectively.

verification. As shown in the constant-current discharge curves of the CF-HPC-2 based symmetric supercapacitor at various specific current values (0.2–5 A g^{-1}) in Fig. 9a, all the curves are nearly symmetrical triangles, indicating the good rate capability of the fabricated device. Fig. 9b shows the CV curves of a symmetric supercapacitor based on CF-HPC-2 at different scan rates from 5 to 100 mV s^{-1}. At different scan rates, a symmetrical rectangular shape was observed in the CV curves.

As shown in Fig. 9c, nearly symmetric triangular shapes can be observed in the GCD curves of CF-HPC-2 conducted under different current densities from 0.5 to 10 A g^{-1}, implying its excellent capacitive behavior. The CV curves exhibit quasi-rectangular shapes from 10 to 200 mV s^{-1}, suggesting that the capacitor exhibits good EDLC behavior and excellent capacitance in 2 M Na_2SO_4 electrolyte (Fig. 9d). The excellent energy density and power density were ascribed to the ordered lamellar

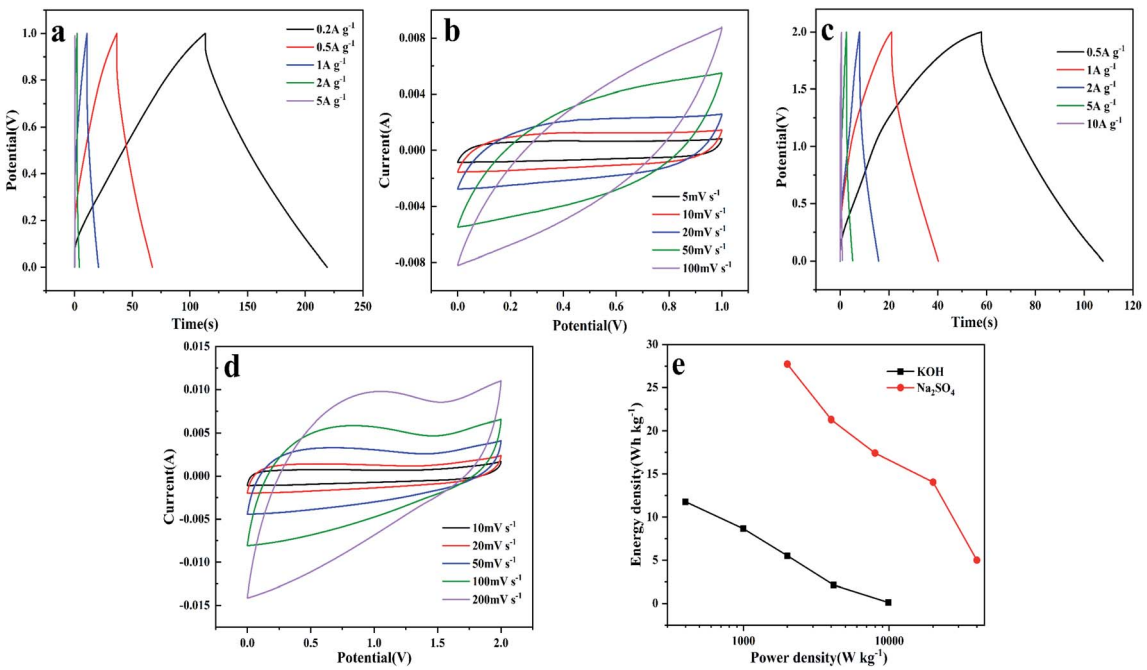

Fig. 9 Electrochemical performance of the CF-HPC-2 based symmetric supercapacitor. (a) GCD and (b) CV curves of CF-HPC-2//CF-HPC-2 at different current densities (0.2–5 A g^{-1}) and scan rates (5–100 mV s^{-1}) in 6 M KOH electrolyte, (c) GCD curves at current densities of 0.5–10 A g^{-1} in 2 M Na_2SO_4 electrolyte, (d) CV curves (10–200 mV s^{-1}) in 2 M Na_2SO_4 electrolyte, and (e) Ragone plots.

Table 3 Comparison of the electrochemical performance of CF-HPC-2 and some reported biomass-derived carbon materials

Precursors	Activator	C_g	C_v	Test conditions	Ref.
Water chestnut	KOH	346	115	6 M KOH, 0.5 A g^{-1}	53
Pomelo peel	$NH_4H_2PO_4/KHCO_3$	207	92.82	0.5 M NaCl, 1 mV s^{-1}	54
Sugar cane bagasse	$ZnCl_2$	300	134	1 M KOH, 0.25 A g^{-1}	55
Kelp	None	440	360	6 M KOH, 0.5 A g^{-1}	56
Flour	LiCl/KCl	261	327	1 M H_2SO_4, 1 A g^{-1}	57
Coconut shell	$ZnCl_2$	248	145.03	6 M KOH, 0.5 A g^{-1}	58
Wheat bran	KOH	294	184	6 M KOH, 0.5 A g^{-1}	59
Acacia gum	KOH	272	177	6 M KOH, 1 A g^{-1}	60
Corn straw	KOH	222	—	6 M KOH, 1 A g^{-1}	61
Shrimp shells	None	322	—	6 M KOH, 0.5 A g^{-1}	62
Fungus	KOH	374	—	6 M KOH, 0.5 A g^{-1}	63
Cycas fluff	$NaHCO_3$	291	349	6 M KOH, 1 A g^{-1}	This work

structure promoting the sufficient storage of ions. The Ragone plot (Fig. 9e) illustrates the energy densities of the CF-HPC-2 based symmetric supercapacitor in 6 M KOH and 2 M Na_2SO_4 electrolytes. The plot shows that the CF-HPC-2 supercapacitor assembly exhibits excellent energy and power densities in Na_2SO_4 compared to in KOH electrolyte. Benefiting from the higher voltage of Na_2SO_4 (2 V), the CF-HPC-2 based symmetric supercapacitor exhibits an energy density of 27.72 W h kg^{-1} at a power density of 20 kW kg^{-1}. Moreover, the energy density remained at 21.31 W h kg^{-1} even as the power density increased to 40 kW kg^{-1}.

4 Conclusion

To sum up, this paper proposes an effective, green and economical strategy by which to prepare layered CF-HPC-*y via* the carbonization and activation of low-cost CF, using mild $NaHCO_3$ as the activator. The optimal activation conditions were investigated by studying the mass ratio of $NaHCO_3$ to CF. The prepared CF-HPC-2 has a high SSA of 516.70 m^2 g^{-1} and a total volume of 0.33 cm^3 g^{-1}. The porous carbon displays a high-volume capacitance of 349.1 F cm^{-3} at 1 A g^{-1} and 289.1 F cm^{-3} at 10 A g^{-1}. Besides this, the energy density of the CF-HPC-2-based symmetric supercapacitor displays a maximum energy density of 27.72 W h kg^{-1} at 20 kW kg^{-1}. Thus, this study proposes a mild and environmentally-friendly method by which to fabricate bulk capacitors, providing a new idea for energy storage systems.

Conflicts of interest

The authors declare that they have no conflicts of interest regarding the publication of this article.

Acknowledgements

The support of the Anhui University Natural Science Research Project (KJ2020A0730), the Anhui Quality Engineering Project (2019jxtd111), The demonstration and leading base for first-class undergraduate talents in materials majors (2020rcsfjd42), the Key project of Natural Science research of Anhui Provincial Department of Education (KJ2019A0675, KJ2021A114, 2021jyxm1507), the National innovation and entrepreneurship program for college Students (202110379034, 202110379038), the Key teaching and scientific research project of Suzhou University (2021yzd07, szxy2021ccjy05, 2020szsfkc1018, 2020ykf07, 2022ykf05), and the Provincial College student innovation and entrepreneurship project (S202110379080, S202110379083, S202110379085, S202110379091, S202110379086) is gratefully acknowledged.

References

1 B. Bayatsarmadi, Y. Zheng, A. Vasileff and S. Z. Qiao, *Small*, 2017, **13**, 1700191.
2 J. W. Nai and X. W. Lou, *Adv. Mater.*, 2019, **31**, 1706825.
3 R. A. Senthil, S. Osman, J. Q. Pan, A. Khan, V. Yang, T. R. Kumar, Y. Z. Sun, Y. J. Lin, X. G. Liu and A. Manikandan, *Colloids Surf., A*, 2020, **586**, 124079.
4 N. S. Wu, J. X. Low, T. Liu, J. G. Yu and S. W. Cao, *Appl. Surf. Sci.*, 2017, **413**, 35–40.
5 X. J. Yang, J. Q. Pan, Y. J. Nie, Y. Z. Sun and P. Y. Wan, *Int. J. Hydrogen Energ.*, 2017, **42**, 26575–26585.
6 Y. Lu, L. Yu and X. W. Lou, *Chem*, 2018, **4**, 972–996.
7 X. Y. Yu and X. W. Lou, *Adv. Energy Mater.*, 2018, **8**, 1701592.
8 L. Y. Zhang, D. W. Shi, T. Liu, M. Jaroniec and J. G. Yu, *Mater. Today*, 2019, **25**, 35–65.
9 G. P. Wang, L. Zhang and J. J. Zhang, *Chem. Soc. Rev.*, 2012, **41**, 797–828.
10 X. X. Liu, C. D. Shi, C. W Zhai, M. L. Cheng, Q. Liu and G. X. Wang, *ACS Appl. Mater. Interfaces*, 2016, **8**, 4585–4591.
11 D. Z. Zhu, J. X. Jiang, D. M. Sun, X. Y. Qian, Y. W. Wang, L. C. Li, Z. W. Wang, X. L. Chai, L. H. Gan and M. X. Liu, *J. Mater. Chem. A*, 2018, **6**, 12334–12343.
12 W. X. Liu, R. L. Yin, X. L. Xu, L. Zhang, W. H. Shi and X. H. Cao, *Adv. Sci.*, 2019, **6**, 1802373.
13 Y. Zhang, Q. Sun, K. S. Xia, B. Han, C. G. Zhou, Q. Gao, H. Q. Wang, S. Pu and J. P. Wu, *ACS Sustainable Chem. Eng.*, 2019, **7**, 5717–5726.
14 G. L. Zhang, T. T. Guan, N. Wang, J. C. Wu, J. L. Wang, J. L. Qiao and K. X. Li, *Chem. Eng. J.*, 2020, **399**, 125818.
15 Z. C. Yang, C. H. Tang, Y. Zhang, H. Gong, X. Li and J. Wang, *Sci. Rep.*, 2013, **3**, 2925.

16 W. C. Jiang, L. Y. Li, J. Q. Pan, R. A. Senthil, X. Jin, J. Q. Cai, J. Wang and X. G. Liu, *J. Power Sources*, 2019, **438**, 226936.
17 G. T. Sun, L. Qiu, M. Q. Zhu, K. Kang and X. H. Guo, *Ind. Crops Prod.*, 2018, **125**, 41–49.
18 S. Witomska, Z. Y. Liu, W. Czepa, A. Aliprandi, D. Pakulski, P. Pawluć, A. Ciesielski and P. Samorì, *J. Am. Chem. Soc.*, 2019, **141**, 482–487.
19 C. Wang, X. F. Wang, H. Lu, H. L. Li and X. S. Zhao, *Carbon*, 2018, **140**, 139–147.
20 Y. Lu, J. N. Liang, S. F. Deng, Q. M. He, S. Y. Deng, Y. Z. Hu and D. L. Wang, *Nano Energy*, 2019, **65**, 103993.
21 E. Raymundo-Piñero, M. Cadek and F. Béguin, *Adv. Funct. Mater.*, 2009, **19**, 1032–1039.
22 F. Y. Liu, Z. X. Wang, H. T. Zhang, L. Jin, X. Chu, B. N. Gu, H. C. Huang and W. Q. Yang, *Carbon*, 2019, **149**, 105–116.
23 G. Z. Zhao, Y. J. Li, G. Zhu, J. Y. Shi, T. Lu and L. K. Pan, *ACS Sustainable Chem. Eng.*, 2019, **7**, 12052–12060.
24 J. Chen, H. M. Wei, H. J. Chen, W. H. Yao, H. L. Lin and S. Han, *Electrochim. Acta*, 2018, **271**, 49–57.
25 J. Guo, D. L. Wu, T. Wang and Y. Ma, *Appl. Surf. Sci.*, 2019, **475**, 56–66.
26 C. X. Cui, Y. Gao, J. Li, C. Yang, M. Liu, H. L. Jin, Z. H. Xia, L. M. Dai, Y. Lei, J. C. Wang and S. Wang, *Angew. Chem., Int. Ed.*, 2020, **59**, 7928–7933.
27 X. S. Zhao, L. C. Yin, T. Zhang, M. Zhang, Z. B. Fang, C. Z. Wang, Y. J. Wei, G. Chen, D. Zhang, Z. H. Sun and F. Li, *Nano Energy*, 2018, **49**, 137–146.
28 X. L. Xing, R. J. Liu, M. Anjass, K. C. Cao, U. Kaiser, G. J. Zhang and C. Streb, *Appl. Catal., B*, 2020, **277**, 119195.
29 P. Wang, G. Zhang, M. Y. Li, Y. X. Yin, J. Y. Li, G. Li, W. P. Wang, W. Peng, F. F. Cao and Y. G. Guo, *Chem. Eng. J.*, 2019, **375**, 122020.
30 J. H. Hou, K. Jiang, R. Wei, M. Tahir, X. G. Wu, M. Shen, X. Z. Wang and C. B. Cao, *ACS Appl. Mater. Interfaces*, 2017, **9**, 30626–30634.
31 L. L. Cheng, Y. Y. Hu, L. Ling, D. D. Qiao, S. C. Cui and Z. Jiao, *Electrochim. Acta*, 2018, **283**, 664–675.
32 L. J. Wang, F. Sun, J. H. Gao, Y. W. Zhu, T. Pei, L. X. Li, G. B. Zhao and Y. K. Qin, *Energ. Fuel.*, 2018, **32**, 9191–9201.
33 L. Pan, X. X. Li, Y. X. Wang, J. L. Liu, W. Tian, H. Ning and M. B. Wu, *Appl. Surf. Sci.*, 2018, **444**, 739–746.
34 S. T. Yang, X. X. Mao, Z. X. Cao, Y. H. Yin, Z. C Wang, M. J. Shi and H. Y. Dong, *Appl. Surf. Sci.*, 2018, **427**, 626–634.
35 X. X. Zhu, X. H. Huang, S. Anwer, N. Wang and L. D. Zhang, *Langmuir*, 2020, **36**, 9284–9290.
36 L. Y. Pang, B. Zou, Y. C. Zou, X. Han, L. Y. Cao, W. Wang and Y. P. Guo, *Colloids Surf., A*, 2016, **504**, 26–33.
37 O. Pezoti, A. L. Cazetta, K. C. Bedin, L. S. Souza, A. C. Martins, T. L. Silva, O. O. S. Júnior, J. V. Visentainer and V. C. Almeida, *Chem. Eng. J.*, 2016, **288**, 778–788.
38 T. M. Darweesh and M. J. Ahmed, *Environ. Toxicol. Pharmacol.*, 2017, **50**, 159–166.
39 M. T. Vu, H. P. Chao, T. V. Trinh, T. T. Le, C. C. Lin and H. N. Tran, *J. Cleaner Prod.*, 2018, **180**, 560–570.
40 M. Mansuer, L. Miao, D. Z. Zhu, H. Duan, Y. K. Lv, L. C. Li, M. X. Liu and L. H. Gan, *Mater. Chem. Front.*, 2021, **5**, 3061–3072.
41 C. L. Long, X. Chen, L. L. Jiang, L. J. Zhi and Z. J. Fan, *Nano Energy*, 2015, **12**, 141–151.
42 H. Chen, S. J. You, Y. Y. Ma, C. Y. Zhang, B. J. Jing, Z. Cai, B. Tang, N. Q. Ren and J. L. Zou, *Chem. Mater.*, 2018, **17**, 6014–6025.
43 V. C. Hoang, V. G. Gomes and K. N. Dinh, *Electrochim. Acta*, 2019, **314**, 49–60.
44 A. Venkatalaxmi, B. S. Padmavathi and T. Amaranath, *Fluid Dyn. Res.*, 2004, **35**, 229.
45 R. Yan, K. Wang, X. D. Tian, X. Li, T. Yang, X. T. Xu, Y. T. He, S. W. Lei and Y. Song, *Carbon Lett*, 2020, **30**, 331–344.
46 M. F. Chen, D. Yu, X. Z. Zheng and X. P. Dong, *J. Energy Storage*, 2019, **21**, 105–112.
47 J. J. Zhou, S. X. Yuan, C. X. Lu, M. H. Yang and Y. Song, *J. Electroanal. Chem.*, 2020, **878**, 114704.
48 S. Ghosh, R. Santhosh, S. Jeniffer, V. Raghavan, G. Jacob, K. Nanaji, P. Kollu, S. K. Jeong and A. N. Grace, *Sci. Rep.*, 2019, **9**, 16315.
49 H. X. Qu, X. J. Zhang, J. J. Zhan, W. Q. Sun, Z. C. Si and H. K. Chen, *ACS Sustainable Chem. Eng.*, 2018, **6**, 7380–7389.
50 M. Mansuer, L. Miao, Y. Qin, Z. Y. Song, D. Z. Zhu, H. Duan, Y. K. Lv, L. C. Li, M. X. Liu and L. H. Gan, *Chin. Chem. Lett.*, 2022, DOI: **10.1016/j.cclet.2022.03.027**.
51 Z. Y. Song, L. Miao, L. Ruhlmann, Y. K. Lv, D. Z. Zhu, L. C. Li, L. H. Gan and M. X. Liu, *Adv. Mater.*, 2021, **33**, 2104148.
52 H. Duan, Z. Y. Song, L. Miao, L. C. Li, D. Z. Zhu, L. H. Gan and M. X. Liu, *J. Mater. Chem. A*, 2022, **10**, 9837–9847.
53 H. M. Wei, J. Chen, N. Fu, H. J. Chen, H. L. Lin and S. Han, *Electrochim. Acta*, 2018, **266**, 161–169.
54 D. Xu, Y. Tong, T. T. Yan, L. Y. Shi and D. S. Zhang, *ACS Sustainable Chem. Eng.*, 2017, **5**, 5810–5819.
55 T. E. Rufford, D. H. Jurcakova, K. Khosla, Z. H. Zhu and G. Q. Lu, *J. Power Sources*, 2010, **195**, 912–918.
56 J. Li, K. Liu, X. Gao, B. Yao, K. F. Huo, Y. L. Cheng, X. F. Cheng, D. C. Chen, B. Wang, D. Ding, M. L. Liu and L. Huang, *ACS Appl. Mater. Interfaces*, 2015, **7**, 24622–24628.
57 Y. X. Hao, F. Xu, M. Qian, J. J. Xu, W. Zhao and F. Q. Huang, *RSC Adv.*, 2017, **7**, 10901–10905.
58 L. Sun, C. G. Tian, M. T. Li, X. Y. Meng, L. Wang, R. H. Wang, J. Yin and H. G. Fu, *J. Mater. Chem. A*, 2013, **21**, 6462–6470.
59 D. W. Wang, Y. G. Min and Y. H. Yu, *J. Solid State Electr.*, 2015, **19**, 577–584.
60 Y. Fan, P. F. Liu, B. Zhu, S. F. Chen, K. L. Yao and R. Han, *Int. J. Hydrogen Energy*, 2015, **40**, 6188–6196.
61 Y. H. Lu, S. L. Zhang, J. M. Yin, C. C. Bai, J. H. Zhang, Y. X. Li, Y. Yang, Z. Ge, M. Zhang, L. Wei, M. X. Ma, Y. F. Ma and Y. S. Chen, *Carbon*, 2017, **124**, 64–71.
62 W. Q. Tian, Q. M. Gao, L. M. Zhang, C. X. Yang, Z. Y. Li, Y. L. Tan, W. W. Qian and H. Zhang, *J. Mater. Chem. A*, 2016, **4**, 8690–8699.
63 C. L. Long, X. Chen, L. L. Jiang, L. J. Zhi and Z. J. Fan, *Nano Energy*, 2015, **12**, 141–151.